4-17-2018

Zika Virus Can Strongly Infect and Disrupt Secondary Organizers in the Ventricular Zone of the Embryonic Chicken Brain

Ankita Thawani

Devika Sirohi

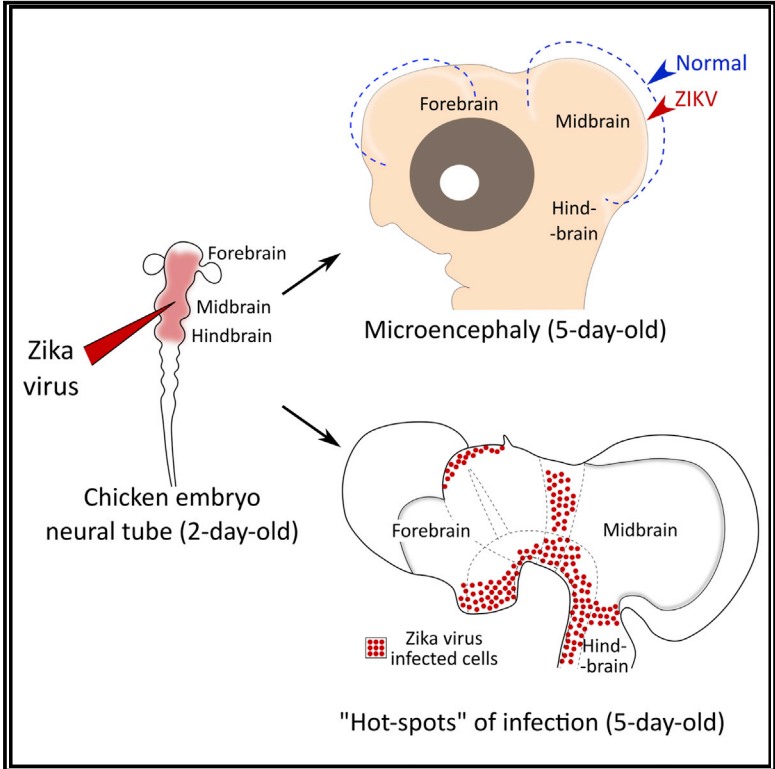Richard J. Kuhn

Donna Fekete

Cell Reports

Zika Virus Can Strongly Infect and Disrupt Secondary Organizers in the Ventricular Zone of the Embryonic Chicken Brain

Graphical Abstract

Authors

Ankita Thawani, Devika Sirohi,
Richard J. Kuhn, Donna M. Fekete

Correspondence

dfekete@purdue.edu

In Brief

Zika virus (ZIKV) displays tropism for neural progenitors. Thawani et al. show non-uniform ZIKV infection in the developing chicken brain, with preferential infection of the basal plate and other sources of key signaling molecules. Cell death within these signaling centers may lead to non-cell-autonomous effects on neighboring neuroepithelial patterning.

Highlights

- Zika virus (ZIKV) infects chicken neural progenitors and causes microencephaly

- ZIKV strongly infects certain brain segments or boundaries (signaling centers)

- ZIKV induces cell death and decreases proliferation within infected regions

- Infected signaling centers show reduced morphogen expression and abated function

CellPress

Zika Virus Can Strongly Infect and Disrupt Secondary Organizers in the Ventricular Zone of the Embryonic Chicken Brain

Ankita Thawani,[1,2,3] Devika Sirohi,[1,3] Richard J. Kuhn,[1,3,4] and Donna M. Fekete[1,2,3,4,5,*]
[1]Department of Biological Sciences, Purdue University, West Lafayette, IN 47907, USA
[2]Purdue Institute for Integrative Neuroscience, Purdue University, West Lafayette, IN 47907, USA
[3]Purdue Institute of Inflammation, Immunology and Infectious Disease, Purdue University, West Lafayette, IN 47907, USA
[4]Purdue University Center for Cancer Research, Purdue University, West Lafayette, IN 47907, USA
[5]Lead Contact
*Correspondence: dfekete@purdue.edu
 https://doi.org/10.1016/j.celrep.2018.03.080

SUMMARY

Zika virus (ZIKV) is associated with severe neurodevelopmental impairments in human fetuses, including microencephaly. Previous reports examining neural progenitor tropism of ZIKV in organoid and animal models did not address whether the virus infects all neural progenitors uniformly. To explore this, ZIKV was injected into the neural tube of 2-day-old chicken embryos, resulting in nonuniform periventricular infection 3 days later. Recurrent foci of intense infection were present at specific signaling centers that influence neuroepithelial patterning at a distance through secretion of morphogens. ZIKV infection reduced transcript levels for 3 morphogens, SHH, BMP7, and FGF8 expressed at the midbrain basal plate, hypothalamic floor plate, and isthmus, respectively. Levels of *Patched1*, a SHH-pathway downstream gene, were also reduced, and a SHH-dependent cell population in the ventral midbrain was shifted in position. Thus, the diminishment of signaling centers through ZIKV-mediated apoptosis may yield broader, non-cell-autonomous changes in brain patterning.

INTRODUCTION

Over 60 years after the Zika virus (ZIKV) was first suspected to infect humans (Dick, 1952), this *Aedes* mosquito-transmitted flavivirus was linked to increased incidences of severe brain defects in fetuses and Guillain Barré syndrome in adults (do Rosário et al., 2016; Rasmussen et al., 2016). ZIKV infection during fetal development causes congenital Zika syndrome, which can present with microencephaly, ventriculomegaly, ocular defects, hearing loss, orthopedic contractures, and intra-uterine growth retardation (de Paula Freitas et al., 2016; Melo et al., 2016; Moore et al., 2017).

Animal models show persistence of ZIKV in the adult brain and testes (Dowall et al., 2016; Lazear et al., 2016). Neural progenitors of the CNS are particularly susceptible to infection in the

adult murine cerebral cortex, human embryonic brain organoids, and the developing brains of murine and nonhuman primates (Li et al., 2016a, 2016b; Miner et al., 2016a; Wu et al., 2016; Yockey et al., 2016). ZIKV infection reduces proliferation and increases cell death of neural stem cells. Ensuing neural defects, like cerebral cortical hypoplasia, glial lesions, and overall embryonic growth restriction, culminate with microencephaly and a higher incidence of fetal lethality (Adams Waldorf et al., 2016; Li et al., 2016a; Miner et al., 2016a; Wu et al., 2016; Yockey et al., 2016). Furthermore, the ZIKV host range was extended to the chicken embryo, where ZIKV was shown to impede brain development and cause ventriculomegaly and embryonic lethality (Goodfellow et al., 2016).

Detailed information about regional specificity for ZIKV infectivity within the early developing brain is currently a knowledge gap. In this study, we exploited the ease of spatiotemporal access in the chicken embryo to explore whether neural progenitors throughout the early developing brain are equally susceptible to ZIKV infection. According to the prosomere model, the embryonic brain is composed of individual anteroposterior (A-P) neuromeres (or brain segments) that are further subdivided into dorsoventral (D-V) compartments. Some of these smaller compartments, or the boundaries between them, are the source of secreted factors (morphogens) that regulate brain patterning from a distance (Echevarría et al., 2003; Puelles and Rubenstein, 2015; Wurst and Bally-Cuif, 2001). By mapping ZIKV infection in different segments of the early developing brain, we identified hotspots of infection at specific neuromeres or neuromere boundaries, many of which are known signaling centers. Three such sites were shown to exhibit reduced morphogen expression when heavily infected, and one is further demonstrated to be accompanied by neural patterning defects. Thus, infection of neuromeres by ZIKV raises the possibility of broader, non-cell-autonomous misregulation in brain development.

RESULTS

ZIKV Replicates in Chicken Embryos and Causes Lethality

Embryonic day 2 (E2) chicken embryos were injected with 10–20 nL ZIKV (9.6 × 10^7 plaque-forming units [PFUs])/mL)
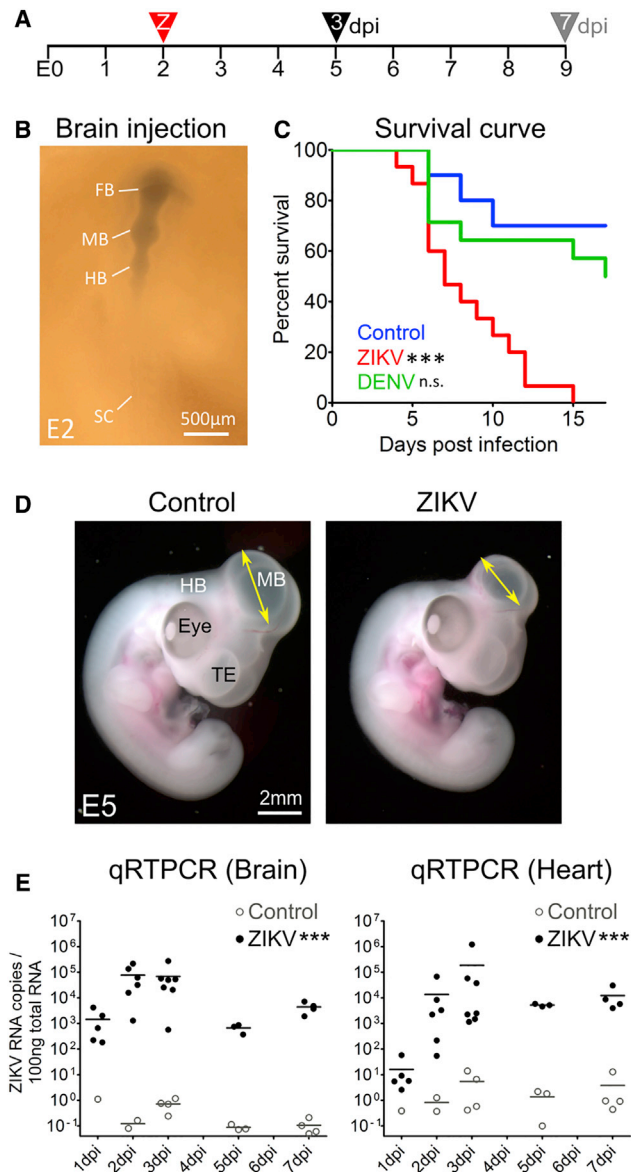
Figure 1. Chicken Embryos Are Permissive to ZIKV, Resulting in a Lethal Infection

(A) Schematic depicting the timing (red arrowhead) of virus (Z) or mock injections and days (3 and 7 dpi, black and gray arrowheads) of histological analysis.

(B) ZIKV inoculum (green hue) into the MB ventricle on E2 spreads to the FB and HB ventricles.

(C) Survival curves for ZIKV, recorded daily, for 10 mock-injected controls, 15 ZIKV, and 14 DENV (log-rank test).

(D) At 3 dpi, the MB diameter (yellow arrows) was smaller in ZIKV-infected embryos.

(E) Real-time qPCR shows the time course of ZIKV viral RNA load in both brain and heart (n = 3–7 embryos; two-way ANOVA; time is also a statistically significant factor by ANOVA). Bar represents the mean.

FB, forebrain; HB, hindbrain; MB, midbrain; TE, telencephalon; Z, ZIKV. ***$p <$ 0.001; n.s., not significant.

delivered to the midbrain (MB) ventricle (Figure 1A). The inoculum spread to the forebrain (FB), MB, and hindbrain (HB) ventricles and often entered the anterior spinal cord (Figure 1B). All ZIKV-injected animals died by 15 days post-infection (dpi; 3–4 days before the anticipated hatching), whereas 70% of the mock-injected controls survived until 17 dpi, when they were terminated; median age of survival was 7 dpi (Figure 1C). In contrast, survival from infection with a non-neurotropic phylogenetic neighbor of ZIKV, Dengue virus, was no different from controls (p = 0.35) (Weaver et al., 2016).

By 3 dpi, the MB and/or FB were visibly smaller in ZIKV embryos than in stage-matched controls (Figure 1D), although the penetrance of microencephaly was variable for both the telencephalon (TE; anterior FB) and the MB lobes (statistical assessment to follow). To assess ZIKV infection and replication, real-time qPCR was performed. ZIKV genomic RNA amplified above the baseline from brains at 1 dpi and from heart by 2 dpi (Figure 1E). In both organs, ZIKV RNA levels peaked around 3 dpi, dropped 30- to 100-fold at 5 dpi, and leveled off at 7 dpi. Thus, we chose to further explore the phenotype at two time points: the approximate peak of viral load (3 dpi) and median age of survival (7 dpi).

ZIKV Infection Reduces the Size of Developing Brain within 3 dpi

The TE and MB areas measured from a lateral projection were reduced by 14% and 16%, respectively, at 3 dpi (Figure 2A). Microcephaly in human infants is measured by head circumference, with "severe" phenotype being over 3 SDs below the mean for a specific age (Ashwal et al., 2009). Using similar criteria for the projected area measurements, 25% of 3 dpi embryos showed a severe reduction in brain size (MB and TE).

By 7 dpi, the surviving 50% of embryos displayed gross morphological abnormalities such as pale epidermis, focal depigmentation in the eye, brain hemorrhages, and/or thoracoabdominal schisis (heart, liver, stomach, intestines outside the body cavity) (data not shown). Average brain wet weight was decreased by 7.6% (Figure 2B). Likewise, the total projected brain area (FB+MB) measured from a dorsal view was 8.3% smaller (Figure 2B). Over one-third (36%) of 7 dpi embryos displayed a severe reduction in brain size (MB+FB).

We used magnetic resonance imaging to determine whether ZIKV infection reduces neuroepithelial thickness or enlarges brain ventricles in the chicken embryo, as it does in humans (Moore et al., 2017). The 5 most severely affected 7 dpi ZIKV brains (from a total of 11) were selected for comparison to 5 randomly selected controls. The average thickness of the TE nuclei was reduced by 15% in ZIKV brains. However, there was no significant change in MB ventricular volume (the site of injection); the variability across ZIKV samples was high (Figure 2C). Figure S1 presents several additional brain measurements at 3 and 7 dpi.

ZIKV Shows a Preference for Specific Neuromeres and Neuromere Boundaries

The localization of ZIKV infection throughout the embryonic brain was done using tissue sections. ZIKV+ cells were labeled with the J2 antibody directed against double-stranded RNA (dsRNA),
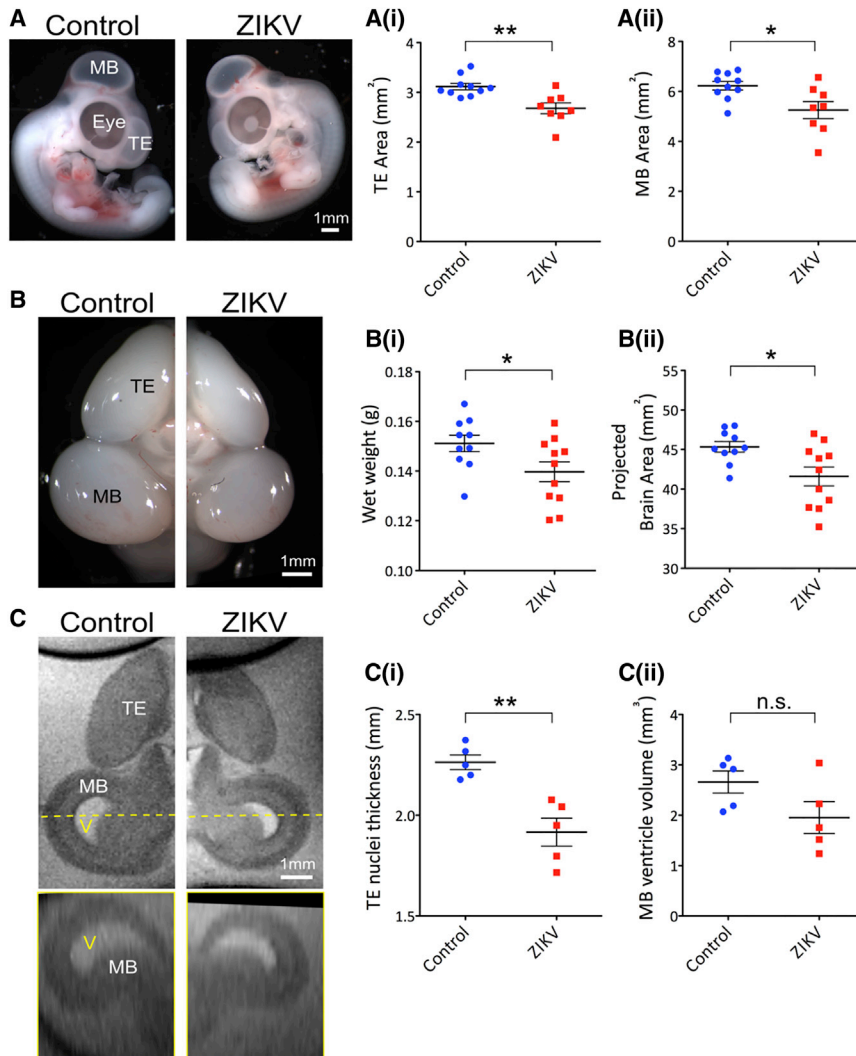
Figure 2. ZIKV Infection Causes Microencephaly in Embryonic Chicken Brain

(A) Projected brain areas were measured from images of 3 dpi whole embryos for the TE area (i) and the MB (ii) area (Figure S1A, areas 2 and 3; n = 10 controls, 8 ZIKV).

(B) At 7 dpi, brain wet weight was determined (i), and then images were used to measure the combined projected brain areas (ii) (Figure S1B, area 6; n = 10 controls, 11 ZIKV).

(C) MRI scans of fixed 7 dpi brains were used to measure TE epithelial thickness (i) and MB ventricle volume (ii; two-tailed t test) (Figure S1C, measure 12 and 15; n = 5 controls, 5 ZIKV).

One-tailed Mann-Whitney test; **$p < 0.01$; *$p < 0.05$; n.s., not significant. Error bars represent mean ± SEM. V, ventricle, and see Figure 1. See also Figure S1.

cord show sporadic infection. Scattered dsRNA labeling in the head mesenchyme and the rest of the body lacked overt spatial preferences (Figure 3B).

ZIKV in Signaling Centers Abates Morphogen Expression Levels and Affects Neural Patterning
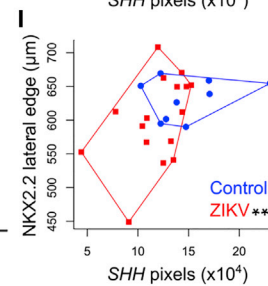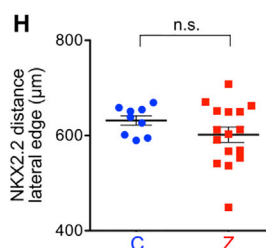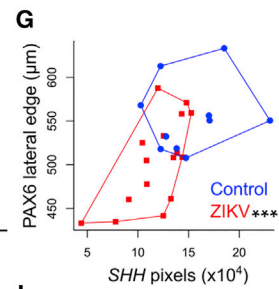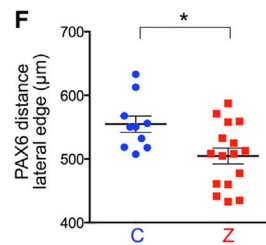
Various neuromeres and neuromere boundaries along both the A-P and D-V axes of the neural tube express evolutionarily conserved secreted morphogens (SHH, BMPS, fgfs, and WNTs) th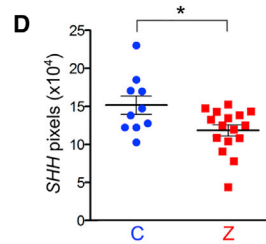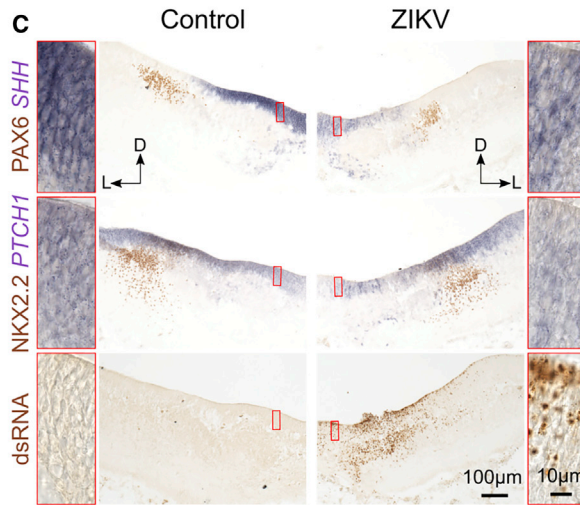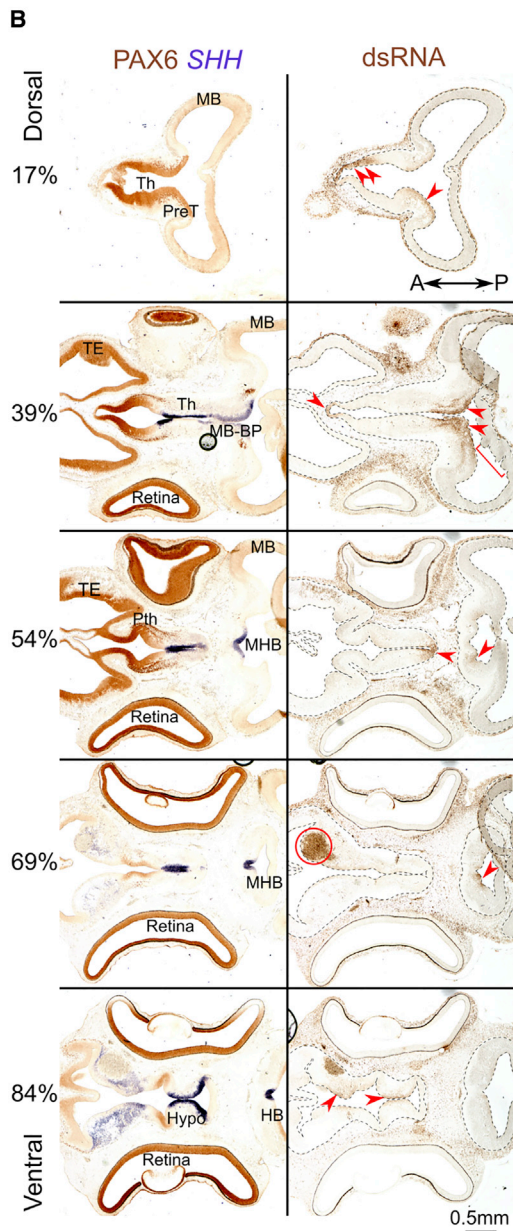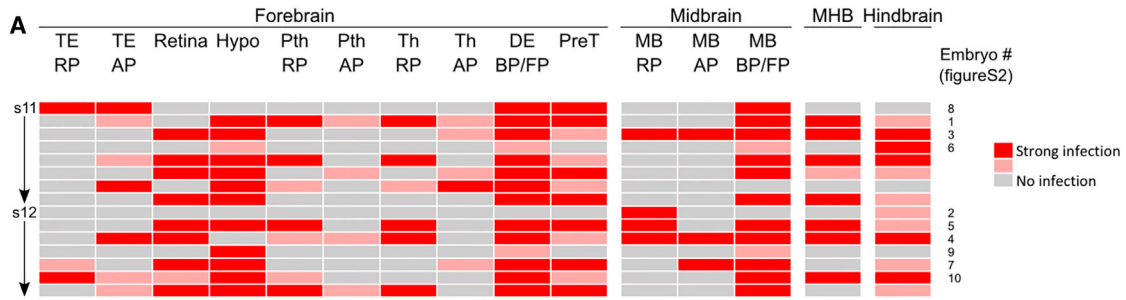at diffuse into the neighboring neuroepithelium and provide fate specification cues to the immature neural tissue. We mapped transcripts of 3 morphogens expressed in the embryonic chicken brain at 3 dpi in areas where ZIKV infection was robust: *SHH* along the floor plate (Perez-Balaguer et al., 2009), *BMP7* at hypothalamic floor plate (Ohyama et al., 2008), and *FGF8B* at the isthmus (Wurst and Bally-Cuif, 2001) as shown in Figure S2D. In the regions with heavy ZIKV infection, these transcripts were reduced as indicated by *in situ* hybridization (Figures 3C and S3A). *SHH* labeling was analyzed quantitatively, whereas *BMP7* and *FGF8* were analyzed qualitatively by a blinded observer with 70%–100% overall agreement achieved (Table S2).

We next sought evidence that morphogen reduction could have a functional impact on brain development, focusing on the MB floor plate at 3 dpi. *Patched1* (*PTCH1*), a downstream effector in the SHH pathway (Marigo and Tabin, 1996), is reduced (Figure 3C; Table S2). At comparable stages of mouse development, the knockout of *SHH* leads to the absence of a PAX6 population in the basolateral MB, and a reduction in an adjacent NKX2.2 population at the alar-basal boundary (Martinez-Lopez et al., 2015; Perez-Balaguer et al., 2009). We hypothesized that, in chicken embryos, a ZIKV-associated reduction of *SHH* expression will either reduce the size or alter the position of the PAX6 and NKX2.2 populations. As expected, *SHH*+ pixel counts were

which is abundantly produced in flavivirus-infected cells (Weber et al., 2006). We expected to find relatively uniform infection in the brain periventricular regions at the early stage of E5 (3 dpi), especially in the MB and TE, given their reduced size (Figures 2 and S1). Instead, there appeared to be a strong preference for ZIKV to infect a few specific regions of the developing brain. Strong dsRNA labeling, or hotspots of infection, was repeatedly found at certain neuromere boundaries and brain subregions (Figures 3A and S2A; Table S1). To better map the ZIKV+ foci, we labeled adjacent sections for evolutionarily conserved genoarchitectural markers such as *SHH* and PAX6 (Ferran et al., 2008; Wurst and Bally-Cuif, 2001). An exemplar specimen shows high ZIKV infection in the hypothalamus, thalamic roof plate, basal plate of the diencephalon (DE) and MB, pretectum, and MB-HB boundary (Figure 3B, red arrows). For a more holistic view of the ventricular/periventricular zone, Figure S2B shows a bisected 3 dpi brain, with robust dsRNA labeling in the pretectum, MB basal plate, MB-HB boundary, and hypothalamus. Figure S2C shows a summary schematic for recurrent regions of infection. Additionally, other regions of the brain and spinal

(legend on next page)

significantly reduced in ZIKV-infected embryos, but this was not accompanied by a significant change in the size of the PAX6 domain (PAX6+ pixels; Figures 3D and 3E). However, the position of the domain was shifted, with the lateral edge of the PAX6 domain located closer to the midline (Figure 3F). The distance of this edge seems to correlate with the size of the *SHH* expression domain, with ZIKV data points located in the lower left quadrant in Figure 3G. Although the NKX2.2 domain was not significantly different in size or position, the lateral edge of the domain shifts medially in a subset of the samples showing reduced *SHH* expression (Figures 3H and 3I). Overall, the data indicate that D-V brain patterning was disrupted by ZIKV-mediated damage to the *SHH*-expressing floor plate.

ZIKV Infection Increased Cell Death and Reduced Cell Proliferation in the Brain

ZIKV-infected cells were mostly located in the periventricular regions that were identified by the densely populated Sox2-expressing progenitors of the ventricular zone and the surrounding intermediate zone of immature neurons (Figures 4A–4D). As expected in the developing brain, phosphohistone-3-positive (pH3+) dividing cells were located along the apical surface of the ventricular zone, where the nuclei reside during M phase of the cell cycle (Misson et al., 1988). Heavily infected regions (dsRNA$^+$) had fewer pH3+ cells and more TUNEL+ labeling (compare Figures 4A and 4B with Figures 4C and 4D). In an exemplar specimen with bilaterally asymmetric ZIKV infection, these changes were particularly striking in a direct comparison of the two sides, with large numbers of fragmented nuclei visible with TUNEL and TO-PRO on the heavily infected side (Figure 4E). Quantitative analysis verified the increase in cell death associated with ZIKV infection (Figures 4F and S3B).

Sensory organs can also be impacted by ZIKV infection, such as chorioretinal atrophy, optic nerve atrophy, and focal pigment mottling in the eye (de Paula Freitas et al., 2016; Miner et al., 2016b; Moore et al., 2017). In 60% of 3 dpi embryos, we observed ZIKV-infected foci in the retina (or the optic nerve), with robust infection correlating with local thinning of the retina, lack of pigmentation (PE), lack of stratification, reduced cell proliferation, increased cell death, and often epithelial delamination (Figure 4G).

At 7 dpi, the medial age of survival, sparse infection remained in the neuroepithelium. Retinal infection was still observed with the aforementioned defects, in addition to frequent infection of extraocular muscles (Figure S4).

DISCUSSION

Like humans, birds can be infected by flaviviruses such as West Nile virus, and hence birds are often used as sentinels for arboviral disease detection (Fair et al., 2011; Langevin et al., 2001). In this study, we investigated the cell and tissue tropism of ZIKV (a flavivirus) in chicken embryos by inoculating them just after closure of the neural tube, a developmental stage comparable to the early 4th week in human gestation (Carnegie stage 11) (Butler and Juurlink, 1987). Although direct ventricular injection does not mimic a natural viral transmission route, our goal was to offer a relatively higher throughput *in vivo* model to study ZIKV pathogenesis. ZIKV caused a productive infection in chicken embryos, as shown previously (Goodfellow et al., 2016). With an inoculum size of 1,000 PFU, lethality reached 100% within 15 dpi, possibly from the neural deficits and/or systemic viremia. The presence of ZIKV in the periventricular region increased cell death, decreased mitotic activity, was sometimes accompanied by reduced expression of the proneural gene Sox2 and could lead to delamination of the neuroepithelium. While periventricular infection and apoptosis were abundant at 3 dpi, very few infected cells were evident 4 days later. This clearance of infected cells is consistent with real-time qPCR data showing that brain viral load fell at 5–7 dpi. In contrast, Dengue virus injection into chicken embryos was not lethal and did not lead to any detectable infection at 3 dpi with anti-dsRNA immunolabeling (data not shown).

Early regionalization and fate specification of the CNS is regulated in part by key signaling centers that are conserved across vertebrates (Ferran et al., 2008; Garcia-Lopez et al., 2009; Puelles and Rubenstein, 2015; Wurst and Bally-Cuif, 2001). For example, the isthmic organizer at the MB-HB boundary regulates formation of the adjacent mesencephalon anteriorly and the cerebellum posteriorly via Wnts and Fgfs (Cavodeassi and Houart, 2012; Echevarría et al., 2003). Similarly, the floorplate expresses *Shh*, and the encoded protein is thought to diffuse dorsally to specify discrete neuronal identities along the D-V

Figure 3. ZIKV Preferentially Infects and Abates Key Signaling Centers in the Developing Brain at 3 dpi

(A) Qualitative analysis of infection at 3 dpi is summarized in the schematic (n = 15). Each row represents an embryo injected with ZIKV at stage (s) 11 or 12.

(B) Alternate sections from a 3 dpi ZIKV-infected embryo (embryo 1 in A) stained for PAX6 (brown), *SHH* (purple), and dsRNA; this example is representative of n = 10 embryos. Some ZIKV infection hotspots are labeled with arrowheads. Relative dorsal-ventral position is indicated by the percentile. Red bracket at 39% shows a peculiar crenellation defect of the neuroepithelium (40% occurrence). Red circle at 69% marks a hemorrhage reflecting diaminobenzidine (DAB) pigment oxidation by endogenous peroxidase in red blood cells.

(C and D) At the MB midline, *SHH* expression is weaker where ZIKV infection is heavy qualitatively (C) and quantitatively (D). *PTCH1*, a gene downstream of SHH, is also weaker in expression (C). Magnified views are shown in the flanking red panels.

(E) PAX6+ pixel count was not changed by ZIKV infection.

(F) The Pax6+ population develops closer to the midline in ZIKV-infected embryos, possibly due to reduced SHH signal (*SHH* pixels) (one-tailed mixed effects SAS model). Left and right sides of each embryo are plotted independently.

(G) Convex hull plot of PAX6 lateral edge against number of *SHH* pixels show ZIKV data in the lower left quadrant of the plot (MANOVA).

(H and I) Although the NKX2.2 population does not show a statistically significant difference in the position of the domain, the convex hull plot shows the cloud of ZIKV data in the lower left quadrant.

***p < 0.001; **p < 0.01; *p < 0.05; n.s., not significant.

Error bars represent mean ± SEM. AP, alar plate; A, anterior; BP, basal plate; D, dorsal; FP, floor plate; Hypo, hypothalamus; L, lateral; MHB, MB-HB boundary; PreT, pretectum; Pth, prethalamus; P, posterior; RP, roof plate; Th, thalamus. See also Figures 1, S2, and S3A and Tables S1 and S2.
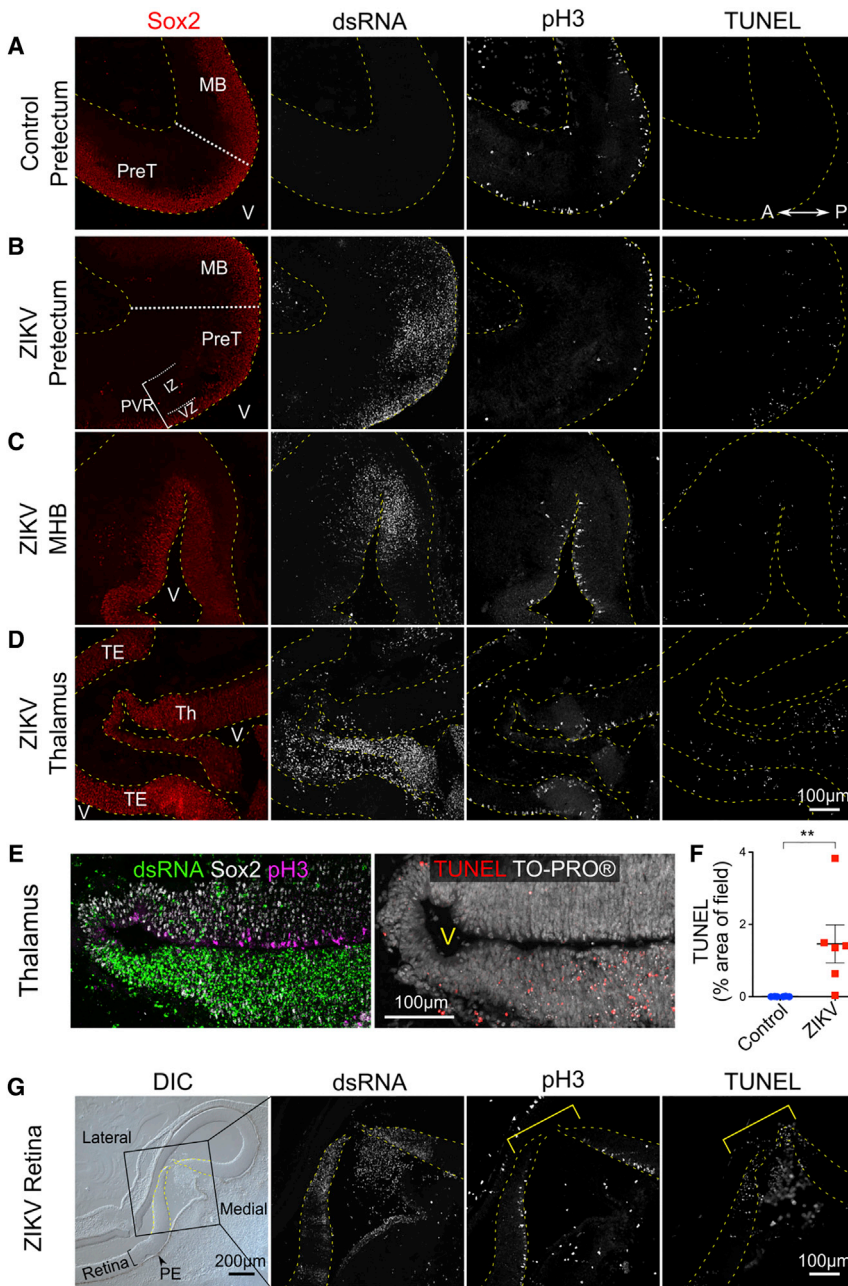
Figure 4. ZIKV Infection Causes Reduced Proliferation and Increased Cell Death

(A–D) Immunostaining at 3 dpi shows ZIKV infection (dsRNA) primarily in Sox2-positive cells of the ventricular zone (VZ) and adjacent intermediate zone (IZ). Regions of high ZIKV infection show fewer pH3+ cells and more TUNEL+ puncta (compare A and B). Other recurring hotspots of infection include MHB (C) and thalamus (D). Sample sizes: dsRNA, n = 15; pH3, n = 6; TUNEL, n = 5.

(E) Dorsal-anterior thalamic section with bilaterally asymmetric infection facilitates a comparison of pH3 and TUNEL labeling under different ZIKV loads. The bottom, heavily infected side (green dsRNA) has fewer pH3+ cells (magenta) at the ventricular surface, more TUNEL+ puncta (red), and more TO-PRO-3+ nuclear fragments (white). Such stark asymmetry of infection was relatively uncommon in our dataset. (B)–(E) correspond to embryo 4 of Figure 3A.

(F) Area occupied by TUNEL+ pixels was quantified at the MB basal plate, a common hotspot of infection (n = 6 controls, 6 ZIKV; one-tailed Mann-Whitney test). Error bars represent mean ± SEM.

(G) Retinal infection is observed in 60% of embryos at 3 dpi (n = 15). High ZIKV infection overlapped with retinal atrophy and delamination (black box in DIC image), low pH3+, and high TUNEL+ signals (yellow bracket). Data correspond to embryo 5 of Figure 3A.

A, anterior; DIC, differential interference contrast; MHB, MB-HB boundary; PE, pigment epithelium; P, posterior; V, ventricle. See also Figures S3B and S4.

compartments (pretectum, isthmus) or reflect D-V compartmentalization (basal plate ventral to the pretectum, thalamic roof plate, hypothalamus). Another hotspot observed less frequently was the dorsal midline (or roof plate) of the MB or TE. The diencephalic regions often showed scattered infection that was much reduced compared to the hotspots. Although there was relatively little infection along the ventricular zone of the dorsal MB, we propose that heavy infection and resulting ZIKV-mediated apoptosis within the neighboring signaling centers could mediate non-cell-autonomous effects on MB development. In support of this idea, in the presence of heavy ZIKV infection, there was a reduction in expression of three morphogens (*SHH*, *BMP7*, and *FGF8*) within three different signaling centers (the MB floorplate, the hypothalamus floorplate and the posterior isthmus, respectively). In the case of SHH bioactivity at the MB basal plate, suggestive evidence of weaker downstream signaling was shown by *PTCH1 in situ* hybridization. However, since *SHH* and *PTCH1* domains partially overlap, it is unclear whether the diminished *PTCH1* expression primarily reflects weaker *SHH* protein levels reaching the responsive cells (i.e., an indirect

axis based on a morphogen model (Echevarría et al., 2003; Perez-Balaguer et al., 2009). Specification of various cell populations, such as dopaminergic and serotonergic neurons of the ventral MB-HB and motor neurons of cranial nerves III–IV, is dependent on patterning cues from the isthmus (A-P signaling center) and the floor plate (*Shh*, D-V signaling center) (Echevarría et al., 2003; Wurst and Bally-Cuif, 2001). Abatement of signaling factors alters the specification or location of neighboring cell populations.

Hence, it was intriguing to discover recurring foci of dense ZIKV infection at several of the morphogen-expressing secondary organizers in our data. Some of these hotspots separate A-P

effect) or whether reduced responsiveness and/or survival of the *PTCH1*-expressing cells could also be contributing factors. We further provide evidence for a neighboring neuroepithelial patterning change in an adjacent PAX6 cell population known to be dependent upon SHH for specification. We do not observe a significant difference in the PAX6 domain size (pixel count). Although direct effects of ZIKV infection on the PAX6 lineage are possible, we observed far less infection within the PAX6+ domain, or in the nearby ventricular zone, in comparison to the *SHH*-expressing domain at the midbrain basal plate. Specifically, the Shh-expressing cells had 4.7 times more infection (dsRNA$^+$ pixels) and 28 times more cell death (TUNEL+ pixels) than the PAX6+ cells (data not shown). A significant change was not observed for the NKX2.2 cell population lateral edge position, possibly because it forms further from the *SHH* basal domain than the PAX6 cells, or because NKX2.2 cells depend on additional morphogens.

In human infants and various animal models, including the chicken embryo, ZIKV exposure causes microencephaly and enlarged brain ventricles (Adams Waldorf et al., 2016; Goodfellow et al., 2016; Moore et al., 2017; Wu et al., 2016). While our study showed size reductions for several brain regions, including the MB, the volume of the MB ventricles was unchanged at 7 dpi; if anything, the average ventricular volume was smaller following ZIKV infection. This discrepancy may be related to differences in the site and timing of ZIKV inoculation, and/or ventriculomegaly might develop from infection during later stages of cortical thickening. Moreover, considering that the MB and TE lobes expand most rapidly during early brain development in the chicken, that we targeted the inoculum to the MB and FB ventricles, and that these structures were obviously reduced by ZIKV injections, we were surprised to find only sparse infection in their respective periventricular regions at 3 dpi and 7 dpi. This leads us to speculate that the growth retardation of these regions might have been indirectly influenced by disruptions in nearby brain structures (such as the secondary organizers).

It remains to be shown whether the regional brain tropism displayed by ZIKV in chicken embryos extends to mammals and whether it can be explained by differential expression of receptors for the virus or other cellular characteristics of signaling centers.

In summary, the chicken embryo is a suitable and self-contained animal model to study the pathogenesis of ZIKV infection in a tissue-specific and temporal manner and potentially to explore therapeutics because of its relative accessibility. Our results suggest that ZIKV exhibits a more nuanced neurotropism than previously appreciated; it preferentially targets specific subpopulations of neural stem cells, particularly some known signaling centers, which leads to reduced morphogen transcripts and alters neural patterning.

EXPERIMENTAL PROCEDURES

Brain Injections

Fresh fertilized White Leghorn chicken eggs (Animal Sciences Research and Education Center, Purdue University), incubated at 37 C–38 C were injected with 1,000–2,000 plaque-forming units (PFU) of ZIKV (H/PF/2013 strain) into the MB ventricles at E2. Some embryos were injected with 500–1,000 PFU Dengue-2 (DENV). Embryos were staged (Hamburger Hamilton [HH] stage; Hamburger and Hamilton, 1951) at the time of injection and harvest. No gender

selection or separate analysis was employed as it is hard to distinguish genders at this early in development. All manipulations of chicken embryos were performed according to NIH guidelines and the policies established by the Purdue University Animal Care and Use Committee. Further details about the virus strains and injections are in Supplemental Experimental Procedures.

Survival Curve

Virus- or mock-injected embryo survival was recorded at the same time every day until E19 (or 17 dpi), when they were terminated before the anticipated hatching. Using GraphPad Prism software, a log-rank test was used to perform pairwise statistical analysis of ZIKV or DENV survival curves compared to mock-injected controls.

Real-Time qPCR

Whole or half brains and whole (E3–E4) or apical (older than E4) heart samples were collected for RNA isolation using Trizol-chloroform and purified with QIAGEN RNAeasy mini kit. Real-time qPCR was performed using SuperScript III Platinum SYBR Green One-Step qPCR Kit w/ROX (Thermofisher Scientific) kit and the primers 5′-CCGCTGCCCAACACAAG-3′ and 5′-CCACTAACGTTCTTTTGCAGACAT-3′. The derived C_t values were converted to the number of ZIKV RNA molecules using a standard curve created using *in-vitro*-transcribed RNA from the ZIKV cDNA (FSS13025 strain) clone (Shan et al., 2016).

Brain Size Quantification

For brain size measurements, whole embryos (3 dpi) or dissected brains (7 dpi) were imaged, and regions of interest were identified (Figure S1). ImageJ was used for measurements by an investigator who was blinded to the experimental group. Selected fixed 7 dpi brains were analyzed by magnetic resonance imaging (MRI) using the 7T Bruker Biospec 70/30 USR small animal scanner with a surface coil receiver at 0.275 mm slice thickness. A middle slice through the FB and MB was used for length measurements (ImageJ, NIH). Using the "Measure Stack" plugin, the volume of the MB ventricle was determined. The "Volume viewer" plugin was used to obtain a tricubic interpolated x-z cross section through the MB for mesencephalic nuclei thickness measurement. Further details about external brain measurements and MRI quantification are in Supplemental Experimental Procedures.

Histology

Samples were fixed, dehydrated, embedded, and cryosectioned. For whole mounts, isolated brains were fixed, dehydrated, and stored at 20 C in methanol. Immunolabeling was performed using primary antibodies against dsRNA, Sox2, PAX6, NKX2.2, or pH3. Details about the antibodies, immunohistochemistry protocols, and co-labeling for cell death with a TUNEL kit can be found in Supplemental Experimental Procedures.

For *in situ* hybridization on cryosections, we used *in-vitro*-transcribed digoxigenin (DIG)-labeled RNA probes to chicken transcripts of interest, followed by alkaline phosphatase detection, as described in Supplemental Experimental Procedures.

Images were acquired using Nikon Eclipse 90i (confocal imaging), Nikon Eclipse E800 (epifluorescence and differential interference contrast [DIC] imaging), or Leica MZFLIII (stereomicroscope). Post-processing of images was performed using ImageJ (NIH) by manipulating brightness and contrast to visualize the signal better; the same adjustment was applied to all the images for a specific marker to prevent bias.

Morphometry

To quantify *SHH*, PAX6, and NKX2.2 domains, double-labeled alternate sections of either *SHH*-PAX6 or *PTCH1*-NKX2.2 were imaged using bright-field microscopy. Pixel numbers and linear measurements for *SHH*, PAX6, and NKX2.2 domains were quantified using ImageJ. One or two middle sections were identified for each left and right sides for quantification.

TUNEL quantification was done using high-resolution confocal images and pixel counts were averaged over 3 to 4 middle sections of the MB basal plate domain.

Detailed ImageJ quantification methodologies are described in Supplemental Experimental Procedures.

Statistics

Scatterplots and survival curves were prepared using GraphPad Prism. Convex hull plots were prepared using RStudio. Statistical Analysis Software (SAS) was used for generating averaged data summaries from raw data points for *Shh*-Pax6 and Nkx2.2 quantification. An unpaired Mann-Whitney t test without assuming the data exhibits Gaussian distribution was performed for statistical analysis of brain size comparisons. For *SHH*-PAX6, and NKX2.2 individual measurement statistical analyses, a mixed effects model was used in SAS with random effect terms to account for correlation between the left and right data points recorded from each embryo. A one-tailed Mann-Whitney test was performed for every measure with the hypothesis that ZIKV causes microencephaly (smaller brains) and reduced genetic markers (*SHH*, PAX6, and NKX2.2), except ventricular volumes, when two-tailed Mann-Whitney test was used because the expected direction of change in ventricular volume was unknown. A multivariate ANOVA (MANOVA) test was used in SAS for *SHH*-PAX6 and *SHH*-NKX2.2 convex hull plot quantification. A two-way ANOVA test was used for real-time qPCR statistical analysis.

SUPPLEMENTAL INFORMATION

Supplemental Information includes Supplemental Experimental Procedures, four figures, and two tables and can be found with this article online at https://doi.org/10.1016/j.celrep.2018.03.080.

AUTHOR CONTRIBUTIONS

Conceptualization, D.M.F., R.J.K., and A.T.; Methodology, D.M.F., A.T., R.J.K., and D.S.; Investigation, A.T. and D.S.; Writing, A.T. and D.M.F.; Funding Acquisition, D.M.F. and R.J.K.

DECLARATION OF INTERESTS

The authors declare no competing interests.

REFERENCES

Adams Waldorf, K.M., Stencel-Baerenwald, J.E., Kapur, R.P., Studholme, C., Boldenow, E., Vornhagen, J., Baldessari, A., Dighe, M.K., Thiel, J., Merillat, S., et al. (2016). Fetal brain lesions after subcutaneous inoculation of Zika virus in a pregnant nonhuman primate. Nat. Med. 22, 1256–1259.

Ashwal, S., Michelson, D., Plawner, L., and Dobyns, W.B.; Quality Standards Subcommittee of the American Academy of Neurology and the Practice Committee of the Child Neurology Society (2009). Practice parameter: Evaluation of the child with microcephaly (an evidence-based review). Neurology 73, 887–897.

Butler, H., and Juurlink, B.H.J. (1987). An atlas for staging mammalian and chick embryos (CRC Press).

Cavodeassi, F., and Houart, C. (2012). Brain regionalization: of signaling centers and boundaries. Dev. Neurobiol. 72, 218–233.

de Paula Freitas, B., de Oliveira Dias, J.R., Prazeres, J., Sacramento, G.A., Ko, A.I., Maia, M., and Belfort, R., Jr. (2016). Ocular findings in infants with microcephaly associated with presumed Zika virus congenital infection in Salvador, Brazil. JAMA Ophthalmol. Published online February 9, 2016. https://doi.org/10.1001/jamaophthalmol.2016.0267.

Dick, G.W. (1952). Zika virus. II. Pathogenicity and physical properties. Trans. R. Soc. Trop. Med. Hyg. 46, 521–534.

do Rosário, M.S., de Jesus, P.A., Vasilakis, N., Farias, D.S., Novaes, M.A., Rodrigues, S.G., Martins, L.C., Vasconcelos, P.F., Ko, A.I., Alcântara, L.C., and de Siqueira, I.C. (2016). Guillain-Barre syndrome after Zika virus infection in Brazil. Am. J. Trop. Med. Hyg. 95, 1157–1160.

Dowall, S.D., Graham, V.A., Rayner, E., Atkinson, B., Hall, G., Watson, R.J., Bosworth, A., Bonney, L.C., Kitchen, S., and Hewson, R. (2016). A susceptible mouse model for Zika virus infection. PLoS Negl. Trop. Dis. 10, e0004658.

Echevarría, D., Vieira, C., Gimeno, L., and Martínez, S. (2003). Neuroepithelial secondary organizers and cell fate specification in the developing brain. Brain Res. Brain Res. Rev. 43, 179–191.

Fair, J.M., Nemeth, N.M., Taylor-McCabe, K.J., Shou, Y., and Marrone, B.L. (2011). Clinical and acquired immunologic responses to West Nile virus infection of domestic chickens (*Gallus gallus domesticus*). Poult. Sci. 90, 328–336.

Ferran, J.L., Sánchez-Arrones, L., Bardet, S.M., Sandoval, J.E., Martínez-de-la-Torre, M., and Puelles, L. (2008). Early pretectal gene expression pattern shows a conserved anteroposterior tripartition in mouse and chicken. Brain Res. Bull. 75, 295–298.

Garcia-Lopez, R., Pombero, A., and Martinez, S. (2009). Fate map of the chick embryo neural tube. Dev. Growth Differ. 51, 145–165.

Goodfellow, F.T., Tesla, B., Simchick, G., Zhao, Q., Hodge, T., Brindley, M.A., and Stice, S.L. (2016). Zika virus induced mortality and microcephaly in chicken embryos. Stem Cells Dev. 25, 1691–1697.

Hamburger, V., and Hamilton, H.L. (1951). A series of normal stages in the development of the chick embryo. J. Morphol. 88, 49–92.

Langevin, S.A., Bunning, M., Davis, B., and Komar, N. (2001). Experimental infection of chickens as candidate sentinels for West Nile Virus. Emerg. Infect. Dis. 7, 726–729.

Lazear, H.M., Govero, J., Smith, A.M., Platt, D.J., Fernandez, E., Miner, J.J., and Diamond, M.S. (2016). A mouse model of Zika virus pathogenesis. Cell Host Microbe 19, 720–730.

Li, C., Xu, D., Ye, Q., Hong, S., Jiang, Y., Liu, X., Zhang, N., Shi, L., Qin, C.F., and Xu, Z. (2016a). Zika virus disrupts neural progenitor development and leads to microcephaly in mice. Cell Stem Cell 19, 120.

Li, H., Saucedo-Cuevas, L., Regla-Nava, J.A., Chai, G., Sheets, N., Tang, W., Terskikh, A.V., Shresta, S., and Gleeson, J.G. (2016b). Zika virus infects neural progenitors in the adult mouse brain and alters proliferation. Cell Stem Cell 19, 593–598.

Marigo, V., and Tabin, C.J. (1996). Regulation of patched by sonic hedgehog in the developing neural tube. Proc. Natl. Acad. Sci. USA 93, 9346–9351.

Martinez-Lopez, J.E., Moreno-Bravo, J.A., Madrigal, M.P., Martinez, S., and Puelles, E. (2015). Mesencephalic basolateral domain specification is dependent on Sonic Hedgehog. Front. Neuroanat. 9, 12.

Melo, A.S., Aguiar, R.S., Amorim, M.M., Arruda, M.B., Melo, F.O., Ribeiro, S.T., Batista, A.G., Ferreira, T., Dos Santos, M.P., Sampaio, V.V., et al. (2016). Congenital Zika virus infection: beyond neonatal microcephaly. JAMA Neurol. 73, 1407–1416.

Miner, J.J., Cao, B., Govero, J., Smith, A.M., Fernandez, E., Cabrera, O.H., Garber, C., Noll, M., Klein, R.S., Noguchi, K.K., et al. (2016a). Zika virus infection during pregnancy in mice causes placental damage and fetal demise. Cell 165, 1081–1091.

Miner, J.J., Sene, A., Richner, J.M., Smith, A.M., Santeford, A., Ban, N., Weger-Lucarelli, J., Manzella, F., Rückert, C., Govero, J., et al. (2016b). Zika virus infection in mice causes panuveitis with shedding of virus in tears. Cell Rep. 16, 3208–3218.

Misson, J.P., Edwards, M.A., Yamamoto, M., and Caviness, V.S., Jr. (1988). Mitotic cycling of radial glial cells of the fetal murine cerebral wall: a combined autoradiographic and immunohistochemical study. Brain Res. *466*, 183–190.

Moore, C.A., Staples, J.E., Dobyns, W.B., Pessoa, A., Ventura, C.V., Fonseca, E.B., Ribeiro, E.M., Ventura, L.O., Neto, N.N., Arena, J.F., and Rasmussen, S.A. (2017). Characterizing the pattern of anomalies in congenital Zika syndrome for pediatric clinicians. JAMA Pediatr. *171*, 288–295.

Ohyama, K., Das, R., and Placzek, M. (2008). Temporal progression of hypothalamic patterning by a dual action of BMP. Development *135*, 3325–3331.

Perez-Balaguer, A., Puelles, E., Wurst, W., and Martinez, S. (2009). Shh dependent and independent maintenance of basal midbrain. Mech. Dev. *126*, 301–313.

Puelles, L., and Rubenstein, J.L. (2015). A new scenario of hypothalamic organization: rationale of new hypotheses introduced in the updated prosomeric model. Front. Neuroanat. *9*, 27.

Rasmussen, S.A., Jamieson, D.J., Honein, M.A., and Petersen, L.R. (2016). Zika virus and birth defects–reviewing the evidence for causality. N. Engl. J. Med. *374*, 1981–1987.

Shan, C., Xie, X., Muruato, A.E., Rossi, S.L., Roundy, C.M., Azar, S.R., Yang, Y., Tesh, R.B., Bourne, N., Barrett, A.D., et al. (2016). An infectious cDNA clone of Zika virus to study viral virulence, mosquito transmission, and antiviral inhibitors. Cell Host Microbe *19*, 891–900.

Weaver, S.C., Costa, F., Garcia-Blanco, M.A., Ko, A.I., Ribeiro, G.S., Saade, G., Shi, P.Y., and Vasilakis, N. (2016). Zika virus: History, emergence, biology, and prospects for control. Antiviral Res. *130*, 69–80.

Weber, F., Wagner, V., Rasmussen, S.B., Hartmann, R., and Paludan, S.R. (2006). Double-stranded RNA is produced by positive-strand RNA viruses and DNA viruses but not in detectable amounts by negative-strand RNA viruses. J. Virol. *80*, 5059–5064.

Wu, K.Y., Zuo, G.L., Li, X.F., Ye, Q., Deng, Y.Q., Huang, X.Y., Cao, W.C., Qin, C.F., and Luo, Z.G. (2016). Vertical transmission of Zika virus targeting the radial glial cells affects cortex development of offspring mice. Cell Res. *26*, 645–654.

Wurst, W., and Bally-Cuif, L. (2001). Neural plate patterning: upstream and downstream of the isthmic organizer. Nat. Rev. Neurosci. *2*, 99–108.

Yockey, L.J., Varela, L., Rakib, T., Khoury-Hanold, W., Fink, S.L., Stutz, B., Szigeti-Buck, K., Van den Pol, A., Lindenbach, B.D., Horvath, T.L., and Iwasaki, A. (2016). Vaginal exposure to Zika virus during pregnancy leads to fetal brain infection. Cell *166*, 1247–1256.